

Excitatory/Inhibitory Balance Emerges as a Key Factor for RBN Performance, Overriding Attractor Dynamics

Emmanuel Calvet^{1,*}, Jean Rouat¹ and Bertrand Reulet²

¹NECOTIS, Faculté de Génie, GEGI, Université de Sherbrooke, Québec, Canada

²Institut Quantique, Faculté des Sciences, Département de Physique, Université de Sherbrooke, Québec, Canada

Correspondence*:

229 Avenue du Mont-Royal Ouest, Montréal, H2T-2T2, Québec, Canada

emmanuel.calvet@usherbrooke.ca

2 ABSTRACT

3 Reservoir computing provides a time and cost-efficient alternative to traditional learning methods.
4 Critical regimes, known as the "edge of chaos," have been found to optimize computational
5 performance in spiking and binary neural networks. However, little attention has been devoted
6 to studying reservoir-to-reservoir variability when investigating the link between connectivity,
7 dynamics, and performance. As physical reservoir computers become more prevalent, developing
8 a systematic approach to network design is crucial. In this article, we examine Random Boolean
9 Networks (RBNs) and demonstrate that specific distribution parameters can lead to diverse
10 dynamics near critical points. We identify distinct dynamical attractors and quantify their statistics,
11 revealing that most reservoirs possess a dominant attractor. We then evaluate performance in
12 two challenging tasks, memorization and prediction, and find that a positive excitatory balance
13 produces a critical point with higher memory performance. In comparison, a negative inhibitory
14 balance delivers another critical point with better prediction performance. Interestingly, we show
15 that the intrinsic attractor dynamics have little influence on performance in either case.

16 **Keywords:** Reservoir Computing, RBN, Criticality, Attractor, Memory, Prediction

1 INTRODUCTION

17 Reservoir Computing (RC) is a promising field for Machine Learning (ML), as the nonlinear reservoir
18 requires no learning and the readout layer only needs linear regression Maass et al. (2002); Jaeger and
19 Haas (2004), reducing time and computational cost Schrauwen et al. (2007). Furthermore, it has potential
20 for real-world implementations as physical reservoirs and dedicated Neuromorphic chips do not always
21 possess the ability to adapt Benjamin et al. (2014); Merolla et al. (2014); Tanaka et al. (2019). Around the
22 same time in 2002, two models were developed: the Liquid State Machine (LSM) Maass et al. (2002) and
23 the Echo State Network (ESN) Jaeger (2001) (rectified version). These approaches differ in their neural
24 models, with LSM using time-event-based neurons and ESNs using Artificial Neural Networks (ANN)

25 with continuous activation functions Jaeger (2001). The Random Boolean Network (RBN) Bertschinger
26 and Natschläger (2004), with binary neurons, is a particularly promising model for LSM and allows for a
27 direct relationship between the reservoir design and its performance in a task Bertschinger and Natschläger
28 (2004); Bertschinger et al. (2004); Snyder et al. (2013). It is widely used to model and implement reservoirs
29 Rosin (2015); Burkow and Tufte (2016); Echlin et al. (2018); Komkov et al. (2021).

30 Studies on the RBN have demonstrated the existence of a phase transition in the dynamics of the reservoir
31 for specific connectivity parameters. Close to the critical regime, an increase in performance in solving
32 various tasks has been reported (boolean logic operations Bertschinger and Natschläger (2004), bit-parity
33 check Bertschinger and Natschläger (2004), prediction of Mackey-Glass time series Canaday et al. (2018)).
34 As of now, most studies in the field of RC rely on phase diagrams to exhibit a statistical relationship
35 between connectivity, dynamics, and performance Bertschinger and Natschläger (2004), Büsing et al.
36 (2010), Snyder et al. (2013), Krauss et al. (2019a), Metzner and Krauss (2022). These results have been
37 obtained by considering a limited number of reservoirs (from one Metzner and Krauss (2022), to 10
38 Bertschinger and Natschläger (2004), up to 100 Krauss et al. (2019b)), and with a limited resolution in
39 terms of the control parameter, due to the computational cost of these phase diagrams.

40 While phase diagrams are essential to comprehend the full range of the computational capabilities these
41 systems can offer, one crucial point is rarely discussed. Since the reservoirs are randomly generated, there
42 might be huge differences between them even though the statistics of their connectivity are the same.
43 Indeed, close to the critical point, reservoir steady-state activities exhibit a wide range of dynamics as
44 discussed by statistical studies Kinouchi and Copelli (2006), Del Papa et al. (2017), Krauss et al. (2019b),
45 and attractor classification Seifert and Reggia (2015), Bianchi et al. (2016), Krauss et al. (2019b), Krauss
46 et al. (2019a), Metzner and Krauss (2022).

47 This article aims at studying the variability of reservoir dynamics, performance, and their correlation.
48 We consider randomly generated RBNs with a single control parameter related to the inhibitory/excitatory
49 balance Krauss et al. (2019a), tuned with high resolution to perform reliable statistical analysis. We study
50 the excitatory/inhibitory balance, attractor dynamics, and performance, and show that the relationship
51 between the three is more complex than previously thought. In line with the work of Metzner and Krauss
52 (2022) on ESN, our research reveals that the RBN also possesses two critical points. Depending on whether
53 the balance is in the majority excitatory or inhibitory, we show that reservoirs respectively exhibit optimal
54 performance in either memory or prediction.

55 The article is organized as follows: in section 2, we describe the model and prove that it is controlled
56 by the ratio of the standard deviation and mean of the weight distribution (noted σ^*), which we use
57 to perform all subsequent analyses. In section 3.1, we show that the sign of σ^* produces two critical
58 regimes. In section 3.2, we classify the activity of free-running reservoirs into four classes according to
59 their attractor dynamics for these two critical regimes. We show that each reservoir can be associated with
60 its most dominant attractor. In section 4.1, we evaluate the relationship between connectivity, dominant
61 attractor, and performance in memory and prediction tasks. We then investigate the relationship between
62 the performances of the two tasks, critical regimes, and dominant attractors in section 4.2. This allows us
63 to derive specific recommendations for simplifying the random generation process of reservoirs. Finally,
64 we discuss our findings in section 5 and their implications for future works in section 6.

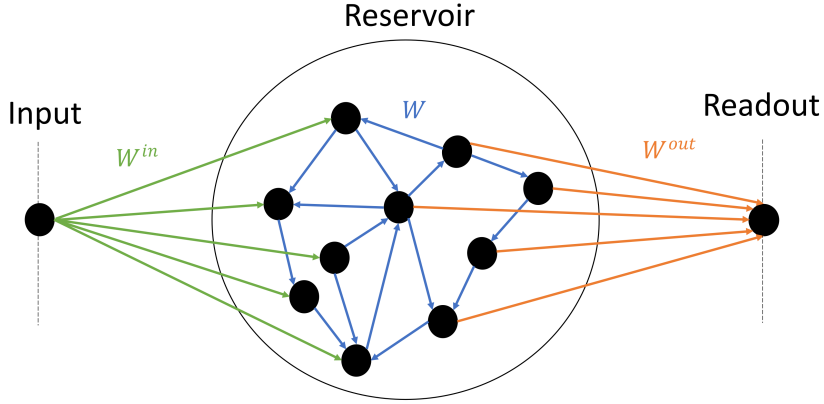


Fig. 1. Schematics of the model. The input node (left) randomly projects synaptic weights to half of the reservoir (center) (green); the reservoir is composed of random recurrent connections (blue); the readout (right) receives input from the other half of the reservoir (orange).

2 MODEL

65 The model consists of one input node, the reservoir itself, and an output node (Fig. 1). Half of the neurons
 66 inside the reservoirs are connected to the input, and the other half to the readout. Thus information between
 67 the input and the readout has to pass through the reservoir. The following subsections describe each
 68 component and how they are interconnected.

69 2.1 The reservoir

70 Phase transitions occur *stricto sensu* only in infinite systems, and critical phenomena are easier to observe
 71 in large systems Lavis et al. (2021). As such, we use an RBN model of size $N = 10,000$ neurons, which is
 72 considerable compared to similar studies in the literature Bertschinger et al. (2004); Büsing et al. (2010);
 73 Metzner and Krauss (2022). The binary state $x_i(t) \in \{0, 1\}$ of the neuron i at the time-step t (with $t \in \mathbb{N}$),
 74 is given by:

$$x_i(t) = \theta \left(u_i(t) + \sum_{j=1}^N w_{ij} x_j(t-1) \right) \quad (1)$$

75 where θ is the Heaviside step function: $\theta(x) = 1$ if $x > 0$ and $\theta(x) = 0$ otherwise. Each neuron receives
 76 the same number of non-zero connections $K = 16$, in the range of values shown to display sharp phase
 77 transitions Büsing et al. (2010). The non-zero recurrent weights of the reservoir w_{ij} (blue arrows in Fig. 1)
 78 are i.i.d. and drawn from the Normal or Gaussian density probability function $\mathcal{N}(\mu, \sigma)$. $u_i(t)$ is the external
 79 input of the neuron i at times t .

80 2.2 Input node

81 The input layer reduces to one node, receiving the time series $u(t)$. The input at times t of a given neuron
 82 i is:

$$u_i(t) = w_i^{in} u(t) \quad (2)$$

83 Where the input weights w_i^{in} (green arrows in Fig. 1) are drawn from a uniform distribution within
 84 $[-0.5, 0.5]$. According to Eq. 1, if the amplitude of the input far exceeds the total contribution of the

85 recurrent weights, then the input mostly controls the dynamics. Our choice of parameters corresponds to an
 86 input of zero average and ~ 0.14 the standard deviation, which is rather low compared to the recurrent
 87 weights. We show in part 4.1 that this choice makes the dynamics mostly controlled by the recurrent
 88 weights, which is the intended behaviour.

89 2.3 Readout

90 The adaptation mechanism is in the output layer only, which reduces here to one linear node with a
 91 sigmoid activation function $f(x) = \frac{1}{1+e^{-x}}$. As such, the output of the network is given by:

$$y(t) = f(\vec{w}^{out} \cdot \vec{x} + c) \quad (3)$$

92 Since all experiments consist in reproducing a unidimensional time series, the output y is a scalar as well.
 93 The column vector \vec{x} represents the state of the reservoir neurons, while the output weights \vec{w}^{out} (orange
 94 arrows in Fig. 1) are stored in a row vector of size N , with half of them set to zero. Lastly, the scalar
 95 c is the bias. The training is performed with a mean square error (MSE) loss function, using standard
 96 ADAM optimizer Kingma and Ba (2015), from the PyTorch library with $\alpha = 0.001$, and 4000 epochs (See
 97 Supplementary Materials 8.2 for more details).

98 2.4 Connectivity: the control parameter σ^*

99 To study the reservoir dynamics, one needs the proper definition of a control parameter. Previous work
 100 on the RBN often focuses on the average and variance of the recurrent weight matrix (Bertschinger and
 101 Natschläger (2004), Bertschinger et al. (2004)). In the following, we demonstrate the existence of only one
 102 control parameter σ^* defined by:

$$\sigma^* = \sigma/\mu, \quad \mu \neq 0 \quad (4)$$

103 Where μ is the mean of the weights and σ their standard deviation. Here we study the reservoir in
 104 the absence of external excitation, $u_i(t) = 0$ in Eq. (1). Let us consider two reservoirs with the same
 105 architecture, the same initial state, and with respective weights matrices W and λW with the scalar $\lambda > 0$.
 106 Since $\lambda > 0$, then $\theta(\lambda x) = \theta(x), \forall x$. Thus, according to Eq. (1) for $u_i(t) = 0$, the two networks are always
 107 in the same state. Thus $(\lambda\mu, \lambda\sigma)$ gives rise to the same time evolution as (μ, σ) . The two corresponding
 108 reservoirs are totally equivalent. We face two cases depending on μ :

- 109 • When $\mu = 0$, choosing $\lambda = 1/\sigma$ leads to the conclusion that all reservoirs $(0, \sigma)$ are strictly equivalent
 110 to the reservoir $(0, 1)$. Hence reservoirs with $\mu = 0$ are independent of σ .
- 111 • When $\mu \neq 0$, choosing $\lambda = 1/|\mu|$ leads to the weights of the second reservoir distributed with a mean
 112 of ± 1 and a standard deviation $\sigma/|\mu|$. Hence we define the control parameter of the RBN as in Eq. (4).

113 Eq. (4) characterizes the distribution of the weights: the mean is the sign of σ^* , and the standard deviation
 114 is its absolute value. Other distribution characterizations directly relate to σ^* . For instance, it is controlling
 115 the balance b between excitation and inhibition, defined by Krauss et al. (2019a) as:

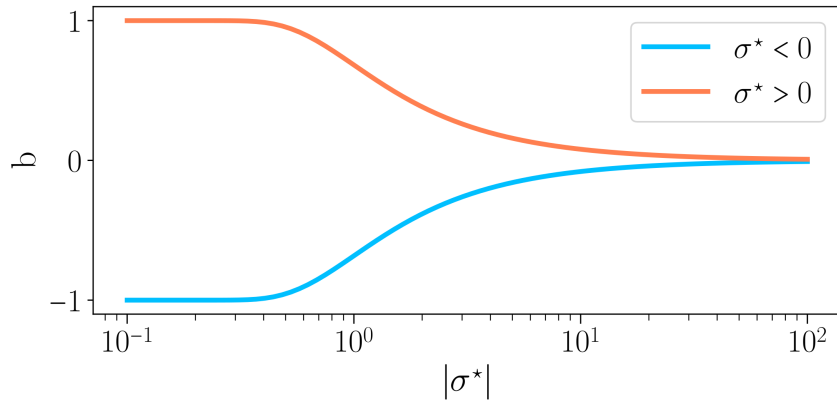


Fig. 2. Excitation/inhibition balance b as a function of the absolute value of the connectivity parameter σ^* , as defined in Eq. 4, for $\sigma^* < 0$ (—) and $\sigma^* > 0$ (—). When the average of weights is positive ($\sigma^* > 0$), whereas the reverse is true when the average of weights is negative.

$$b = (S_+ - S_-)/S \quad (5)$$

$$S_{\pm} = \frac{S}{2}(1 \pm b) \quad (6)$$

With $S = S_+ + S_- = KN$ the total number of synapses, S_- the number of inhibitory synapses ($w_{ij} < 0$), and S_+ the number of excitatory synapses ($w_{ij} > 0$). By taking a normal weight distribution, the number of excitatory synapses is given by:

$$S_+ = S \int_0^{+\infty} \frac{1}{\sqrt{\pi}} e^{-\left(x - \frac{\mu}{\sqrt{2}\sigma}\right)^2} dx \quad (7)$$

By substituting Eq. (7) in Eq. (6), we find $b = \text{Erf}[1/(\sqrt{2}\sigma^*)]$, with Erf the error function. Thus, by controlling the weight distribution, our control parameter σ^* drives the excitatory to inhibitory balance and thus the reservoir dynamics, in line with Krauss et al. (2019b) and Metzner and Krauss (2022). Fig. 2 shows the relationship between b and σ^* . The case $\mu = 0$ corresponds to $b = 0$ (perfect balance between excitation and inhibition) and $\sigma^* \rightarrow \infty$, for any value of σ . For $\sigma^* < 0$, $b \in [-1, 0]$, i.e. there is a majority of inhibitory synapses while for $\sigma^* > 0$, $b \in [0, 1]$, hence a majority of excitatory synapses.

In the following, we will use σ^* as the unique control parameter (in the range of values displayed in supplementary material S8).

3 STATISTICS OF DYNAMICS AT THE CRITICAL POINTS

The importance of neural networks dynamics in understanding their performances has been widely explored (Bertschinger and Natschläger (2004), Büsing et al. (2010), Krauss et al. (2019a), Metzner and Krauss (2022)). The purpose of this part is to investigate the relationship between connectivity and dynamics through two statistical analyses:

- 131 1. **Activity statistics:** In section 3.1, we analyze the statistics of the neural activity as a function of the
 132 control parameter σ^* . We demonstrate the existence of two critical points and characterize them.
 133 2. **Reservoirs attractors:** In section 3.2, we classify the steady state time evolution of the network
 134 activity into four distinct attractors and study the influence of the initial state and random weight
 135 generation. We show that reservoirs possess a dominant attractor independent of initial conditions.

136 **3.1 Statistics of the activity of free-evolving reservoirs**

137 **3.1.1 Methodology:**

138 The first experiment is a free evolution of reservoirs in the absence of input, i.e. $u_i = 0$. We define the
 139 network activity as $A(t) = \sum_i x_i(t)/N$, with N the number of neurons in the reservoir, and $A \in [0, 1]$. A
 140 is also the proportion of excited neurons: $A = 0$ if the network is extinguished ($x_i = 0 \quad \forall i$), $A = 1$ if the
 141 network is saturated ($x_i = 1 \quad \forall i$). At the initial state, we randomly force 20% of neurons to an up state
 142 ($x_i = 1$), i.e. $A(t=0) = 0.2$. After a transient regime of 1000 time steps, the reservoir reaches a steady
 143 state where we perform statistics. In the following, A will refer to the activity measured in that steady state
 144 (see supplementary material S9 for a more formal definition). For each value of σ^* , we perform statistics on
 145 100 randomly generated reservoirs (see supplementary material S7.1 for more details on the experiment).

146 **3.1.2 Analysis:**

147 In the following, a bar over a variable $(\bar{\cdot})$ represents an average over time for a given reservoir, while
 148 the brackets $\langle \cdot \rangle$ represents an average over different randomly generated reservoirs. In the first analysis,
 149 we calculate the time-average steady activity \bar{A} for a given reservoir and its time-variance $\overline{\delta A^2}$, where we
 150 define $\delta A = A - \bar{A}$. We average these quantities over the reservoirs to give $\langle \bar{A} \rangle$ and $\langle \overline{\delta A^2} \rangle$ for each value
 151 of σ^* . Next, we evaluate the average and variance over reservoirs of the binary entropy H_b , or BiEntropy
 152 Croll (2013) of the time-dependent activity. Compared to the Shanon entropy, the advantage of this metric
 153 is that it can discriminate ordered from disordered strings of binary digits. It has been used in machine
 154 learning Mamun et al. (2016), Zhou and Zeng (2022), but to our knowledge, this is the first time in reservoir
 155 computing. The binary entropy varies between 0 for fully ordered bit-streams and 1 for fully disordered
 156 ones. We compute the BiEntropy of the binarized time dependence of the steady activity for each reservoir
 157 (for the exact definition of all the metrics, see S10).

158 **3.1.3 Results:**

159 The time-average activity $\langle \bar{A} \rangle$ as a function of σ^* is shown in Fig. 3A, for both signs of σ^* (Fig. 2). The
 160 green dashed line represents the value obtained for $\mu = 0$, i.e. $\sigma \rightarrow \infty$. The perfect balance in excitation
 161 ($b = 0$) results in half of the neurons being activated $\langle \bar{A} \rangle = 0.5$. The variance $\langle \overline{\delta A^2} \rangle$ vs σ^* is shown in
 162 Figs. 3B. For the lowest values of $|\sigma^*|$, the reservoirs are frozen (zero variance) either extinguished (for
 163 $\sigma^* < 0$) or saturated ($\sigma^* > 0$). This corresponds to reservoirs being respectively purely inhibitory ($b = -1$)
 164 or excitatory ($b = 1$). Already at the level of the statistics of the activity, there is a clear difference between
 165 both signs of σ^* : for $\sigma^* < 0$ there is a threshold in σ^* (vertical dashed line at $\sigma^* \sim -0.7$) above which the
 166 average activity and its variance rise abruptly and simultaneously. In contrast, for $\sigma^* > 0$, there is a wide
 167 region where no dynamic is detected (zero variance), yet the network is not saturated but its activity decays
 168 continuously. The variance starts rising at $\sigma^* > 4$ (vertical dash-dotted line).

169 The average BiEntropy $\langle H_b \rangle$ vs. $|\sigma^*|$ is plotted in Figs. 3B for $\sigma^* > 0$ and 3D for $\sigma^* < 0$ (left scale,
 170 black stars on both plots). These two plots zoom in the vicinity of the phase transition, as statistics are
 171 stationary elsewhere. There is a continuous transition between a fully ordered phase ($\langle H_b \rangle = 0$) and a

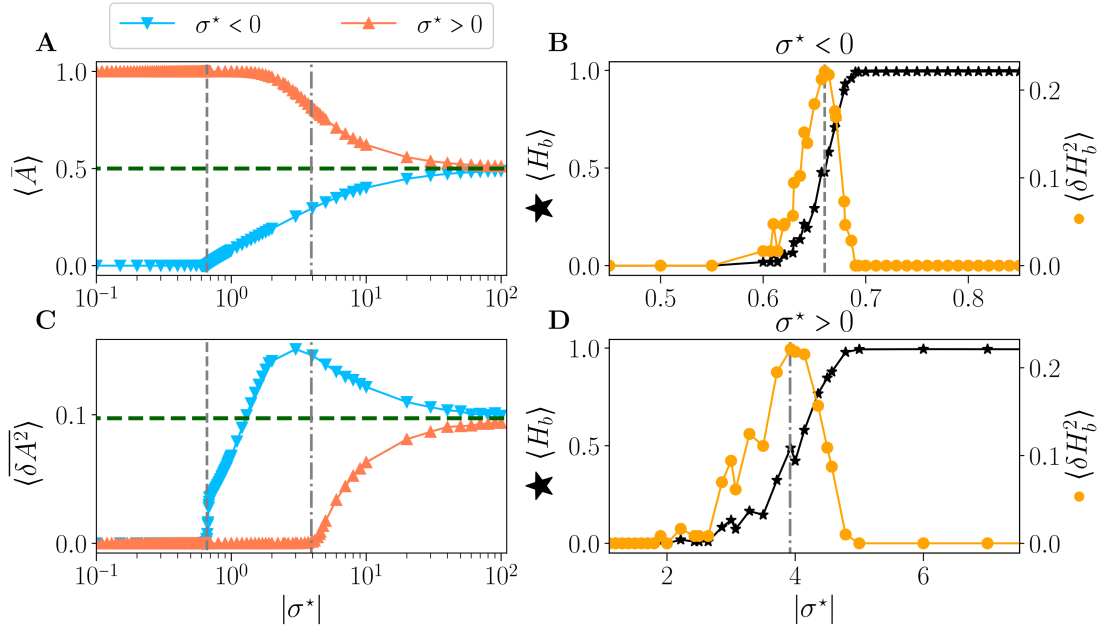


Fig. 3. Statistics of the activity of free running reservoirs in the steady state as a function of $|\sigma^*|$. Average over reservoirs of time average activity $\langle \bar{A} \rangle$ (A), and average over reservoir of time variance $\langle \delta \bar{A}^2 \rangle$ (C), for $\sigma^* < 0$ (▼) and $\sigma^* > 0$ (▲). In all plots, the gray vertical lines represent the critical values of the control parameter for $\sigma_c^* < 0$ (---) and $\sigma_c^* > 0$ (----). B and D zoom on the region of interest close to the critical points: average over reservoirs of BiEntropy $\langle H_b \rangle$ (*, left scale) and BiEntropy variance $\langle \delta H_b^2 \rangle$ (●, right scale), for $\sigma^* < 0$ (B) and $\sigma^* > 0$ (D).

fully disordered one ($\langle H_b \rangle = 1$). Since the BiEntropy is a measure of order, these results suggest that the transition we observe is related to the apparition of chaos in the reservoir above a critical value of σ^* (Lewin and Bak (1993), Bertschinger and Natschläger (2004), Seifter and Reggia (2015), Kuśmierz et al. (2020)). The variance of the BiEntropy $\langle \delta H_b^2 \rangle$ is shown in Figs. 3B for $\sigma^* > 0$ and 3C for $\sigma^* < 0$ (right scale, orange circles on both plots). It is zero when either in the ordered or disordered phase and spikes at the transition. Its maximum coincides with $\langle H_b \rangle \simeq 0.5$: the variance of BiEntropy captures the edge of chaos as a balance between order and disorder. More striking, it also coincides with the position at which the variance of the activity rises (vertical dashed lines). The peak of $\langle \delta H_b^2 \rangle$ thus provides a clear definition of the position of two critical points: $\sigma_c^* \simeq -0.66$ and $\sigma_c^* \simeq 4.0$, which correspond respectively to critical balances $b_c \simeq -0.87$ (94% of inhibitory synapses) and $b_c \simeq 0.19$ (60% of excitatory synapses). Moreover, the transition between order and disorder is much wider for $\sigma^* > 0$. This asymmetry between both signs of σ^* is a property of our model since $\theta(-x) \neq \pm\theta(x)$ in Eq.(1). From now on, we will refer to the *critical points* as the point where the maximum of BiEntropy variance is obtained, and we will define the *critical regions* as the regions with $\langle \delta H_b^2 \rangle \neq 0$.

3.1.4 Discussion:

Similar to Krauss et al. (2019b) and Metzner and Krauss (2022), the existence of phases separated by critical points as a parameter is varied is reminiscent of the phase diagrams drawn in thermodynamics. If we associate the state of a neuron, 0 or 1, to the state of an Ising spin, either down or up, then $\langle \bar{A} \rangle$ corresponds to the average magnetization per spin of the network and $\langle \delta \bar{A}^2 \rangle$ to the variance of its fluctuations, i.e. magnetization noise. At equilibrium, it is proportional to the magnetic susceptibility according to the

192 fluctuation-dissipation theorem Callen and Welton (1951). The total magnetization plays the role of an order
193 parameter, and the transition order is obtained by considering discontinuities, as a function of temperature,
194 of the order parameter and its derivatives with respect to the external field L. D. Landau (1980). Here
195 we observe that the average activity is always continuous as a function of σ^* . At the same time, $\langle \delta A^2 \rangle$ is
196 continuous for $\sigma^* > 0$ but shows a discontinuity at the critical point for $\sigma^* < 0$. This strongly suggests that
197 the two "phase transitions" are of a different type.

198 **3.2 Dominant attractor of reservoirs**

199 In the previous section, we considered the *average* behaviour of reservoirs: for a given value of σ^* we
200 averaged over many realizations of the distribution of synaptic weights. However, from a practical point of
201 view, one wants to use one network to work with different inputs. This raises two questions: that of the
202 reservoir-to-reservoir variability (do all reservoirs behave similarly?) and that of the sensitivity of a given
203 reservoir to initial conditions. We address these questions in this section.

204 **3.2.1 Methodology:**

205 We submitted our reservoirs again to a free evolution without input ($u_i(t) = 0$). For each value of σ^* ,
206 we created 100 reservoirs with randomly tossed weight matrices. Each reservoir is run 100 times, with a
207 different random initial state, of activity $A(t=0) = 0.2$ (for more details, see *Statistics of reservoirs* in
208 S7).

209 **3.2.2 Analysis:**

210 We classify the attractor obtained in the steady-state activities, as proposed in Krauss et al. (2019b). We
211 categorize the activity signals into one of the four types of attractors (see S11 for a grounded justification
212 of each category):

- 213 • *Extinguished* activity: The steady-state activity $A(t)$ is always zero. This means that the initial activity
214 died during the transient phase and that the reservoir could not propagate it further in time. For
215 simplicity, we will sometime refer to it as *dead* attractor.
216 • *Fixed* point attractor: The steady-state reservoir is active ($A(t) \neq 0$), but the activity is independent of
217 time ($\delta A(t) = 0$). This includes the *saturated* states $A(t) = 1$ of ref. Seifert and Reggia (2015).
218 • *Cyclic* attractor: $A(t)$ is periodic with a periodicity larger than one time-step.
219 • *Chaotic* attractor: $A(t)$ is neither constant nor periodic.

220 We determine the attractor obtained at the steady state for each reservoir and initial condition. We then
221 compute the distribution of attractors for each value of σ^* obtained overall the initial conditions of all
222 reservoirs. The statistics are thus computed on 10,000 steady activities for each σ^* .

223 **3.2.3 Results:**

224 Fig. 4A-F provide examples of attractors, encoded in the colours, for each reservoir (x-axis) and each
225 initial condition (y-axis) for different values of σ^* . The left column (blue-bordered boxes) corresponds to
226 values below the critical point (vertical blue lines on Figs. 4G,H), the center column (gray-bordered boxes)
227 to values at the critical point (vertical gray lines), and the right column (red-bordered boxes) to values
228 above the critical points (vertical red lines). The upper row displays negative σ^* values, while the lower
229 row features positive σ^* values.

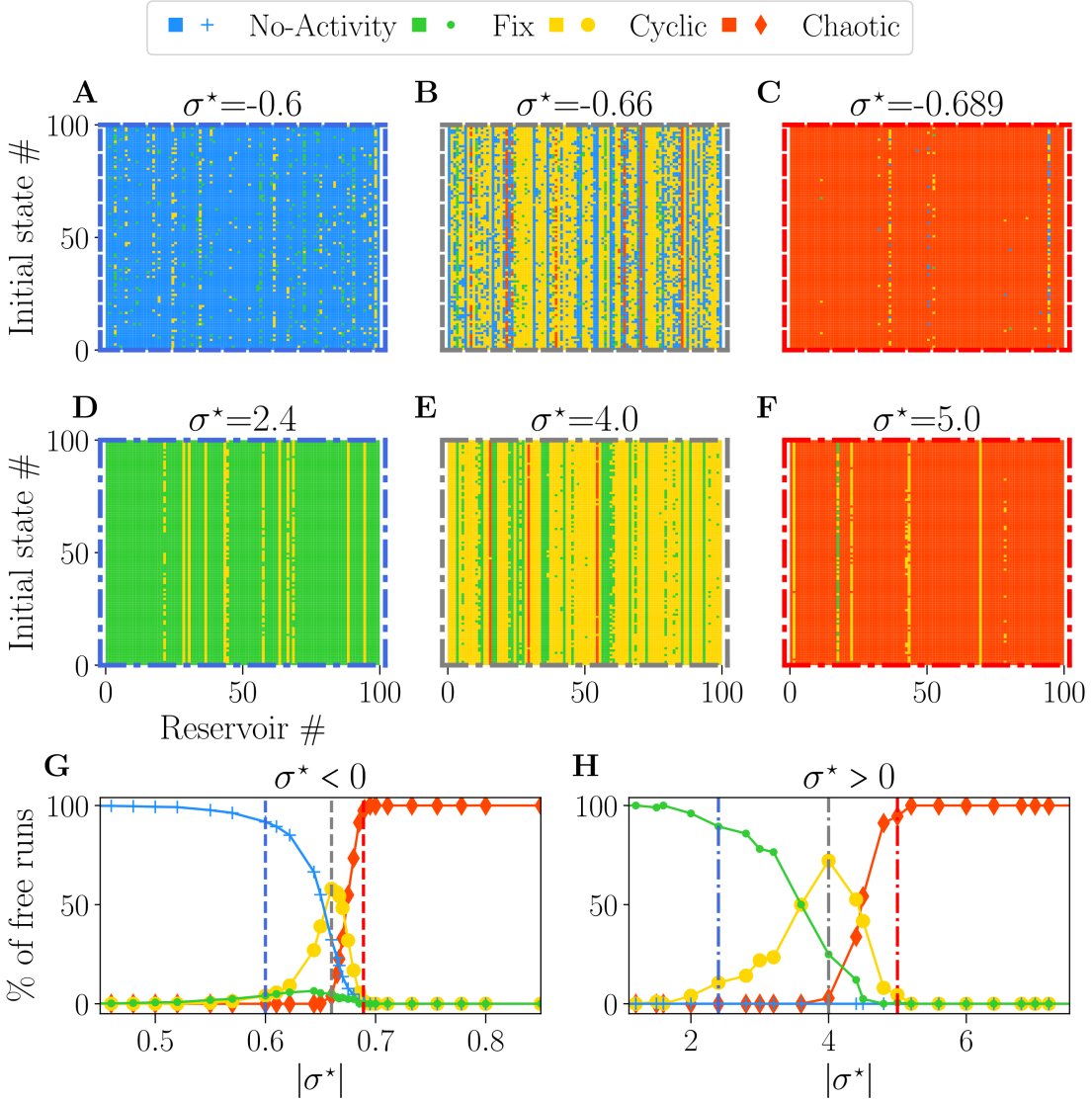


Fig. 4. The attractor landscape of reservoirs: for $\sigma^* < 0$ (**A, B, C, G**), and for $\sigma^* > 0$ (**D, E, F, H**). The influence of initial conditions for specific values of σ^* : (**A**) $\sigma^* = -0.6$, (**B**) $\sigma^* = -0.66$, (**C**) $\sigma^* = -0.689$, (**D**) $\sigma^* = 2.4$, (**E**) $\sigma^* = 4.0$, (**F**) $\sigma^* = 5.0$. In each plot, the vertical axis represents different numbers (#) of initial random states of free-running reservoirs. The horizontal axis represents different numbers (#) of reservoirs with various initial weight tossing, randomly generated with distinct seeds. Pixels of colours represent the attractor obtained at the steady state, with the same colours as (**G, H**). **G, H:** percentage of steady-state activities belonging to each category of attractors: no-activity (+), fix (•), cyclic (○), and chaotic (♦), for $\sigma^* < 0$ (**G**) and $\sigma^* > 0$ (**H**). In each row (**A, B, C**) and (**E, F, G**), the coloured dashed boxes surrounding the plots correspond to the values of σ^* , indicated as vertical lines in plots **G** and **H**.

230 Away from the critical point, a dominant colour is observed, meaning that reservoirs exhibit a dominant
 231 attractor. Steady activities are predominantly extinguished and fixed on the left side of the critical point (**A**,
 232 **C**) and chaotic at the right (**D, F**). Close to the critical points (**B** and **E**), there is an increase in the diversity
 233 of attractors, as previously observed Karimipanah et al. (2017).

234 Fig. 4.G and H show the statistical distribution of all obtained attractors versus $|\sigma^*|$. As expected from
 235 the previous analysis, there is no attractor diversity on the far left and right of the plots, as we obtain
 236 one primary attractor. Dead (blue line) or fixed (green line) attractors are found for low values of $|\sigma^*|$,

237 and their proportion decays slowly across the transition. Within the critical region coexist all attractors
238 in various proportions. Chaotic attractors start to appear precisely at the transition (vertical gray lines),
239 while the domain where cyclic attractors exist coincides with the critical region of nonzero BiEntropy
240 variance (Fig. 3.B,D). The point at which cyclic attractors are most present is also precisely σ_c^* . These
241 results corroborate what we inferred in the previous section: on the disordered phase $|\sigma^*| > |\sigma_c^*|$, attractors
242 are chaotic, while the ordered phase is characterized by fixed or dead attractors. We note an asymmetry
243 between both sides of the transition: chaotic attractors appear only in the disordered phase. From the point
244 of view of the attractors, both signs of σ^* lead to similar behaviours, except again, that the transition region
245 is much wider for $\sigma^* > 0$.

246 3.2.4 Discussion:

247 Our results suggest that the critical points enhance sensitivity to the initial states and configuration of
248 the weights, explaining the reservoir-to-reservoir variance and increase in dynamic diversity. Reservoirs
249 around the negative σ_c^* (Fig. 4.B) possessed a distribution of attractors with far more variety than the one
250 with positive σ_c^* (Fig. 4.E), further reinforcing the idea that the sign of σ^* produces two distinct types
251 of critical regimes. We quantified this in the supplementary material S12 by computing the entropy of
252 reservoir attractor distributions plotted in Fig. 8. We interpret that result by suggesting that inhibition might
253 be a key factor for enhancing dynamic diversity.

254 For the purpose of reservoir design, our findings suggest that with both critical points, most reservoirs
255 possess an attractor obtained predominantly in most trials, independent of the initial state. The statistics of
256 dominant reservoir attractors are presented in supplementary Fig. 8, and found to be similar to the one in
257 Fig. 3. The presence of vertical colour lines in Fig. 4A-F means that, in most cases, the behaviour of the
258 reservoirs does not depend on the initial state, even in the critical region (this is more thoroughly shown
259 in the supplementary material S12). As a consequence, a dominant attractor can be associated with each
260 reservoir, irrespective of the initial condition.

4 WHAT DRIVES PERFORMANCES

261 In this section, we examine whether there is a relationship between reservoir dynamics in the absence of
262 input, as explored in the previous section, and its ability to perform two demanding tasks: memory and
263 prediction. This is done in two steps:

- 264 • **Connectivity, attractor, and performance:** In section 4.1, we analyze the performance obtained
265 separately in each task, depending on the control parameter, for each dominant attractor category. We
266 show that the key factor driving performance is the excitatory/inhibitory balance.
- 267 • **Attractor and cross-task performance:** In section 4.2, we analyze all reservoir performances
268 independently of the control parameter. For each reservoir, we study the relationship between the
269 performance obtained in each task and their dominant attractor. This allows us to deduce how to
270 generate a reservoir for the best general purpose.

271 From now on, and for ease of notation, a reservoir with a dominant attractor obtained during free evolution
272 (defined in previous section 3.2) will be referred to as either: a *extinguished*, *fix*, *cyclic*, or *chaotic* reservoir
273 (e.g., an *extinguished reservoir* refers to a reservoir with an extinguished dominant attractor).

274 4.1 Performance in memory and prediction tasks

275 Close to the critical points, we obtained various dominant attractors for a single value of σ^* . This raises
 276 an important question regarding the relationship between the dominant attractor of a reservoir and its
 277 performance. Specifically, it is worth investigating whether the dominant attractor influences the reservoir's
 278 performance. If this is the case, grouping attractor categories by discrete performance levels may be
 279 possible based on a single value of σ^* .

280 4.1.1 Methodology:

281 We evaluate the performance of the networks to execute two fundamental tasks: *memory* and *prediction*.
 282 Each reservoir receives an input $u(t)$, and the readout target is $T(t) = u(t + \delta)$, equal to the input shifted
 283 in time by δ time steps. $\delta < 0$ corresponds to a memory task, and $\delta > 0$ to a prediction task. For each value
 284 of σ^* , we use 100 reservoirs, and each reservoir is run five times, with a different random tossing of the
 285 input weight matrix (more detail on the training procedure in S8.2).

286 The first task consists of memorizing a purely random signal (i.e., uncorrelated white noise), and since
 287 there is absolutely no correlation in the input, only memorization is involved. Fig. 5.A illustrates this task
 288 for one value of $\delta = -6$, with white noise as input u , and the target T .

289 For the second task, we explore the ability of the reservoir to predict a time series, $\delta = 10$ time steps in
 290 the future. The input is the well-known Mackey-Glass time series, as it is a common benchmark of this type
 291 of task (Hajnal and Lörincz (2006), Goudarzi et al. (2016), Canaday et al. (2018), among others), notably
 292 testing the ability to infer non-linear dynamics. The signal regularity is controlled by the parameter τ , see
 293 Fig. 5.B, ranging from periodic with $\tau = 5$, to chaotic for $\tau = 28$ (more information on the experiments in
 294 S8.1).

295 4.1.2 Analysis:

296 The performance of a reservoir is measured by computing the correlation product $Corr(y, T)$ between
 297 the output y and the target T . A perfect match corresponds to a correlation of one, while a random output
 298 gives a zero correlation. An individual reservoir performance score is then obtained by averaging over the
 299 initial conditions. Each individual reservoir is associated with its dominant attractor, and the statistics of
 300 the performance of reservoirs are performed separately for each attractor.

301 4.1.3 Results:

302 The average performance is plotted as a function of $|\sigma^*|$ in Fig. 5.C,E for the memory task and in Fig. 5.D,F
 303 for the prediction task. The left column (**C** and **D**) corresponds to $\sigma^* > 0$, and the right column (**E** and **F**)
 304 to $\sigma < 0$. The colour of the lines corresponds to the attractor.

305 For $\sigma^* < 0$ (Fig. 5.E and F), performance increases over a very wide range of σ^* , both for memory
 306 and prediction. This range includes the critical region (gray hatched area) but is vastly broader. Thus,
 307 being within the critical region is absolutely not mandatory to perform well. A shaded area in Figs. 5
 308 indicates the spreading of the results. There is none in plots C and D, meaning that all reservoirs perform
 309 exactly the same for a given σ^* . Moreover, as σ^* is increased through the critical region, the dominant
 310 attractors change, but there is no discontinuity in the performance (see zooms in plot E and F): this strongly
 311 suggests that the dynamics of the reservoir, as measured in the absence of input, is irrelevant for the
 312 performance. Only the value of σ^* matters. In both tasks, the average performance decreases monotonically
 313 with increasing difficulty via τ and δ . In the memory task, we register a dip in performance close to the
 314 critical point. This goes against the common assumption that the edge of chaos is optimal for memory

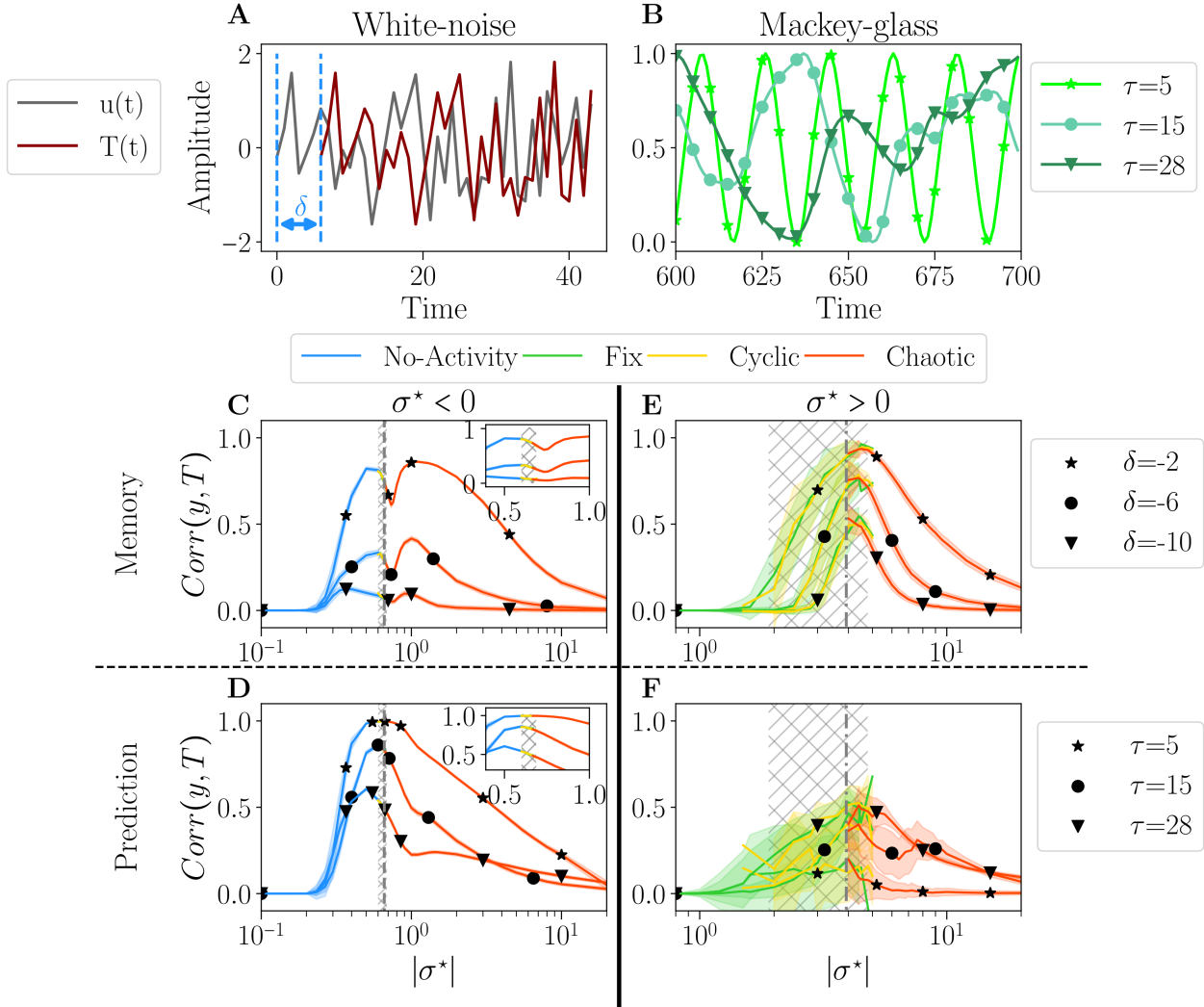


Fig. 5. Performances for two tasks: white noise memory (**C, E**); and Mackey-glass prediction (**D, F**). **A** and **D**: examples of signals for each task with their respective parameters. **A**: White noise memory task, which consists in remembering the input (gray), to reproduce it in output (dark red) with a negative delay δ (shown example corresponds to $\delta = -6$). **B**: Mackey glass is controlled by the parameter τ (see methodology 8.1 for more details), ranging from periodic to chaotic. **C, D, E, F**: the average performance $\text{Corr}(y, T)$ between the output y and target T , plotted over $|\sigma^*|$, for each dominant attractor category: *no-activity*, *fix*, *cyclic* or *chaotic*. The shaded area represents one standard deviation. Higher correlations indicate better performance. The hatched gray area represents the critical regions, as defined in section 3.1. **C** and **D**: the performance in the white-noise memory task; three values of δ are tested: -2 (\star), -6 (\bullet), -10 (\blacktriangledown). **E** and **F**: the performance of Mackey-Glass prediction ($\delta = +10$); three values of τ are tested: 5 (\star), 20 (\star), 50 (\blacktriangledown). **C** and **D**: Performance for $\sigma^* < 0$, with inside each plot a zoom on the critical region. **E** and **F**: performance for $\sigma^* > 0$.

315 Bertschinger et al. (2004). In the prediction task, the peak of performance roughly coincides with the
 316 critical region, except for the greater difficulty, where the peak is slightly on the left.

317 The picture is very different for $\sigma^* > 0$ (Figs. 5E and F). First, the region in which some level
 318 of performance is observed is comparable to the critical region observed in free-running reservoirs.
 319 Second, there is substantial variability in performance across different reservoirs, as indicated by the large
 320 shaded areas. Despite this variability, there is an overall dependence of performance on σ^* . The average

321 performance of distinct dominant attractor categories is much noisier, but there is still no evidence that the
322 attractor category has any significant impact on the reservoir's performance. We observe that performance
323 decreases as the difficulty of the memorization task increases, but interestingly, this trend appears to be
324 inverted in the prediction task.

325 Once again, the two signs of σ^* give rise to different behaviour. In particular, networks with $\sigma^* > 0$
326 memorize better and are less reliable than those with $\sigma^* < 0$ but have poorer prediction capability.

327 **4.1.4 Discussion:**

328 Our results somewhat challenge the common assumption that the edge of chaos is optimal for performance
329 and suggest that this is true for reservoirs with a majority of excitation but not necessarily with a majority
330 of inhibition. Reservoirs with negative σ^* exhibit very reliable performances with very low reservoir-to-
331 reservoir variability over a range in σ^* much broader than the critical region. Since reservoirs behave the
332 same, in practice, it is sufficient to generate one, with σ^* at the left of the critical region. However, if the
333 goal is optimal memorization, it is wiser to choose $\sigma \sim 0.4$ in the critical region and try different reservoirs
334 until finding a good one, which requires training and testing.

335 **4.2 Cross-task performance**

336 Beyond studying the performance in memorization and prediction separately, as often done (Bertschinger
337 and Natschläger (2004), Büsing et al. (2010)), here we aim at answering the following question: are the
338 reservoirs intrinsically good or bad, or does it depend on the task? In other words, are there general-purpose
339 reservoirs and specialized ones?

340 **4.2.1 Analysis:**

341 We analyze the absolute value of the performance of all reservoirs independently of the control parameter.
342 For each reservoir, we study its performance in the memory task as a function of its performance in the
343 prediction tasks (see section 4.1 *methodology*). For this, we fixed values of δ (memory) and τ (prediction),
344 and we chose three levels of difficulty: simple ($\tau = 5, \delta = -2$), average ($\tau = 20, \delta = -6$) and difficult
345 ($\tau = 28, \delta = -10$).

346 **4.2.2 Results:**

347 Fig. 6 displays the performance of reservoirs as coloured dots. As in the previous section, each colour
348 corresponds to the dominant attractor of the reservoir. The vertical axis represents the performance in the
349 prediction task (Mackey-Glass), and the horizontal axis that of the memory task (white noise). The columns
350 correspond to the sign of σ^* , negative on the left, positive on the right. The rows correspond to the degree
351 of difficulty, from simple (top) to difficult (bottom).

352 For $\sigma^* < 0$ (left column), there is an apparent relationship in performance between the two tasks. The
353 degree of difficulty roughly acts as a scaling factor on the curves, but the correlation is always clear. The
354 reservoirs which are good at predicting do memorize well as well. There is, however, a reentrant region of
355 chaotic reservoirs (red) which are the best at memorizing but are not optimal for predicting, in particular for
356 the intermediate degree of difficulty (see the red loop on Fig. 6B). This point corresponds to the maximum
357 on the right of the dip observed in Fig 5C. Interestingly, in all difficulties, reservoirs at the critical point
358 (encircled dots) create a narrow area with a good overall performance.

359 The picture is very different for $\sigma^* > 0$ (right column). Performances are distributed as clouds of points.
360 In Fig. 5, we observe a large reservoir variability in both tasks. Some reservoirs are suitable for one task

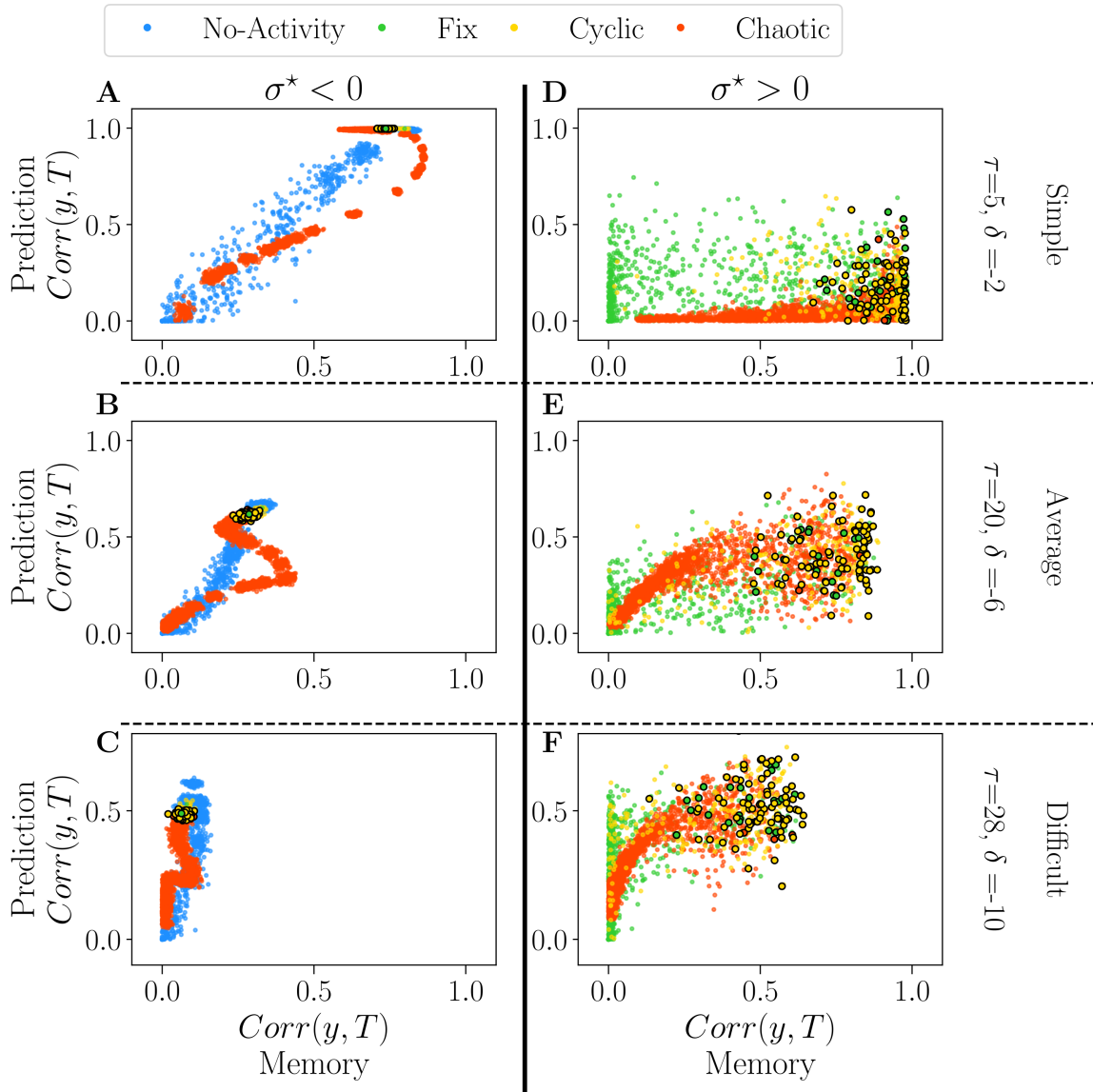


Fig. 6. The performance of all reservoirs in the prediction tasks (Mackey-Glass) as a function of their performance in the memory tasks (white-noise), for $\sigma^* < 0$ (**A**, **B**, **C**) and $\sigma^* > 0$ (**D**, **E**, **F**). Reservoirs are again classified according to their dominant attractor (see supplementary material S13). In all plots, dots with black edges display reservoirs taken at the critical regimes. We chose three different pairs of values for the parameters of the tasks, τ and δ , each representing a different difficulty level: 1. Simple (**A** and **D**) the lowest difficulty in both tasks, $\tau = 5$ and $\delta = -2$; 2. Average (**B** and **E**) average difficulty for intermediary values of $\tau = 20$ and $\delta = -6$; 3. Difficult (**C** and **F**) difficult task for higher values of $\tau = 28$ and $\delta = -10$.

361 and bad for the other one. For intermediate and difficult tasks, some reservoirs outperform the best ones
 362 with $\sigma^* < 0$ in both memorization and prediction. Reservoirs at the critical point are found on the right of
 363 the plots, i.e. they promise good memorization but are nonetheless widely spread, especially in prediction
 364 (vertical axis).

365 4.2.3 Discussion:

366 Correlations in performances are very different for both signs of σ^* . Choosing a reservoir with $\sigma^* \sim$
 367 -0.66 ensures a good, general-purpose reservoir but with suboptimal performance. In contrast, going

368 into the positive side of σ^* may lead to the best reservoirs in a given task or even better general purpose
369 reservoirs, but this comes at a price: those gems cannot be found by the statistical analysis we have
370 performed on their free running activity.

5 CONCLUSION

371 This article aimed at investigating the relationship between connectivity, dynamics, and performance in the
372 design of RBN reservoirs. We demonstrated that the only control parameter is the ratio $\sigma^* = \sigma/\mu$ through
373 a Gaussian weight distribution, which indirectly regulates the excitatory/inhibitory balance. We found two
374 critical points, and observed that reservoirs typically possess a dominant attractor, regardless of their initial
375 states.

376 We investigated the relationship between the performance, the control parameter, and the preferred
377 attractor in memory and prediction tasks. Our results reveal that σ^* , hence the excitatory-inhibitory balance
378 b , has a strong impact on performance while the dynamics of the attractor have none. We showed how to
379 select a control parameter region that ensures good performance, thus providing a very efficient way to
380 obtain high performance reservoirs. This region corresponds to high attractor diversity. For $\sigma < 0$, the
381 critical region is narrower and does not necessarily coincide with the top of performance, while for $\sigma > 0$,
382 the critical region corresponds to the performing region.

383 For the tasks, we showed that negative σ^* values produced superior results in prediction, with reliable
384 performance and low reservoir-to-reservoir variability. Therefore, it is sufficient to perform free-running
385 and pick a single value of σ^* , preferably close to the critical point σ_c^* . In contrast, positive σ^* values were
386 found to have higher performance in memory tasks but with greater volatility. Since a given σ^* value can
387 lead to diverse performance outcomes, generating random reservoirs and testing them during training to
388 select the best performers is still necessary. Given enough trials, however, our findings suggest that $\sigma^* > 0$
389 can generate the bests general-purpose reservoirs.

6 FUTURE WORK

390 The limited impact of the intrinsic attractor dynamics on performance may result from the broadness of
391 the attractor categories. Future work with refined categories may reveal greater performance sensitivity to
392 attractor dynamics. For example, the extinguished category included all reservoirs with activities dying
393 before 1000 time steps. Refining the analysis could involve correlating performance with the average time
394 before free-running reservoir activity dies out. Similarly, cyclic reservoirs could be refined by analyzing
395 their period, while some chaotic activities may be considered cyclic when run for more extended periods.
396 Moreover, it is possible that combining other types of measures, such as correlation in space and time, as
397 performed in Metzner and Krauss (2022), could provide better categorization of dynamics, with ultimately
398 better predictive power of performance.

ACKNOWLEDGEMENT

399 EC extends gratitude to Matin Azadmanesh, Lucas Herranz, and Ismael Balafrej for critical reading of the
400 manuscript. The authors also express their appreciation to their colleagues at NECOTIS for their valuable
401 feedback and insightful discussions throughout the research process.

AUTHOR CONTRIBUTIONS

402 This article represents the collaborative effort of EC, JR, and BR. EC conducted the research under the
403 supervision of JR and BR. EC created the model, collected and analyzed the data, and wrote the manuscript.
404 JR provided invaluable guidance and perspective throughout the process, and BR contributed to the writing
405 and revision of the manuscript. All authors read and approved the final version of the article.

FUNDING

406 This work was supported by the CRSNG/NSERC, the Canada First Research Excellence Fund, and the
407 QsciTech program.

REFERENCES

- 408 Benjamin, B. V., Gao, P., McQuinn, E., Choudhary, S., Chandrasekaran, A. R., Bussat, J.-M., et al. (2014).
409 Neurogrid: A Mixed-Analog-Digital Multichip System for Large-Scale Neural Simulations. *Proceedings*
410 *of the IEEE* 102, 699–716. doi:10.1109/JPROC.2014.2313565
- 411 Bertschinger, N. and Natschläger, T. (2004). Real-time computation at the edge of chaos in recurrent neural
412 networks. *Neural Computation* 16, 1413–1436. doi:10.1162/089976604323057443
- 413 Bertschinger, N., Natschläger, T., and Legenstein, R. (2004). At the edge of chaos: Real-time computations
414 and self-organized criticality in recurrent neural networks. In *Advances in Neural Information Processing*
415 *Systems*, eds. L. Saul, Y. Weiss, and L. Bottou (MIT Press), vol. 17
- 416 Bianchi, F. M., Livi, L., and Alippi, C. (2016). Investigating echo state networks dynamics by means
417 of recurrence analysis. *IEEE transactions on neural networks and learning systems* 29, 427–439.
418 doi:10.1109/TNNLS.2016.2630802
- 419 Blackledge, J. M. and Mosola, N. (2020). A Statistically Significant Test to Evaluate the Order or
420 Disorder of a Binary String. In *2020 31st Irish Signals and Systems Conference (ISSC)* (IEEE), 1–6.
421 doi:10.1109/ISSC49989.2020.9180178
- 422 Burkow, A. V. and Tufte, G. (2016). *Exploring Physical Reservoir Computing using Random Boolean*
423 *Networks*. Ph.D. thesis, Norwegian University of Science and Technology - NTNU
- 424 Büsing, L., Schrauwen, B., and Legenstein, R. (2010). Connectivity, dynamics, and memory in reservoir
425 computing with binary and analog neurons. *Neural Computation* 22, 1272–1311. doi:10.1162/neco.
426 2009.01-09-947
- 427 Callen, H. B. and Welton, T. A. (1951). Irreversibility and Generalized Noise. *Physical Review* 83, 34.
428 doi:10.1103/PhysRev.83.34
- 429 Canaday, D., Griffith, A., and Gauthier, D. J. (2018). Rapid time series prediction with a hardware-based
430 reservoir computer. *Chaos* 28, 1–13. doi:10.1063/1.5048199
- 431 Cohen, O., Keselman, A., Moses, E., Rodríguez Martínez, M., Soriano, J., and Tlusty, T. (2010). Quorum
432 percolation in living neural networks. *EPL (Europhysics Letters)* 89, 18008. doi:10.1209/0295-5075/89/
433 18008
- 434 Coniglio, A., Nappi, C. R., Peruggi, F., and Russo, L. (1976). Percolation and phase transitions in the Ising
435 model. *Communications in Mathematical Physics* 51, 315–323. doi:10.1007/BF01617925
- 436 Croll, G. J. (2013). Bientropy - the approximate entropy of a finite binary string. *CoRR* abs/1305.0954
- 437 Del Papa, B., Priesemann, V., and Triesch, J. (2017). Criticality meets learning: Criticality signatures in a
438 self-organizing recurrent neural network. *PLoS ONE* 12, 1–21. doi:10.1371/journal.pone.0178683

- 439 Echlin, M., Aguilar, B., Notarangelo, M., Gibbs, D., and Shmulevich, I. (2018). Flexibility of Boolean
440 Network Reservoir Computers in Approximating Arbitrary Recursive and Non-Recursive Binary Filters.
441 *Entropy* 20, 954. doi:10.3390/e20120954
- 442 Goudarzi, A., Marzen, S., Banda, P., Feldman, G., Teuscher, C., and Stefanovic, D. (2016). Memory and
443 Information Processing in Recurrent Neural Networks 0, 1–8
- 444 Hajnal, M. A. and Lörincz, A. (2006). Critical echo state networks. *Lecture Notes in Computer Science*
445 (*including subseries Lecture Notes in Artificial Intelligence and Lecture Notes in Bioinformatics*) 4131
446 LNCS, 658–667. doi:10.1007/11840817{_}69
- 447 Hämäläinen, M., Hari, R., Ilmoniemi, R. J., Knuutila, J., and Lounasmaa, O. V. (1993). Magnetoen-
448 cephalography theory, instrumentation, and applications to noninvasive studies of the working human
449 brain. *Reviews of Modern Physics* 65. doi:10.1103/RevModPhys.65.413
- 450 Hopfield, J. J. (1982). Neural networks and physical systems with emergent collective computational
451 abilities. *Proceedings of the National Academy of Sciences of the United States of America* 79. doi:10.
452 1073/pnas.79.8.2554
- 453 Ising, E. (1925). Beitrag zur Theorie des Ferromagnetismus. *Zeitschrift für Physik* 31. doi:10.1007/
454 BF02980577
- 455 [Dataset] Jaeger, H. (2001). The “echo state” approach to analysing and training recurrent neural networks-
456 with an erratum note’. doi:10.24406/publica-fhg-291111
- 457 Jaeger, H. and Haas, H. (2004). Harnessing Nonlinearity: Predicting Chaotic Systems and Saving Energy
458 in Wireless Communication. *Science* 304. doi:10.1126/science.1091277
- 459 Karimipanah, Y., Ma, Z., and Wessel, R. (2017). Criticality predicts maximum irregularity in recurrent
460 networks of excitatory nodes. *PLOS ONE* 12, e0182501. doi:10.1371/journal.pone.0182501
- 461 Kingma, D. P. and Ba, J. (2015). Adam: A Method for Stochastic Optimization. In *3rd International
462 Conference for Learning Representations, San Diego*
- 463 Kinouchi, O. and Copelli, M. (2006). Optimal dynamical range of excitable networks at criticality. *Nature
464 Physics* 2, 348–351. doi:10.1038/nphys289
- 465 Komkov, H., Pocher, L., Restelli, A., Hunt, B., and Lathrop, D. (2021). RF Signal Classification using
466 Boolean Reservoir Computing on an FPGA. *Proceedings of the International Joint Conference on
467 Neural Networks* 2021-July. doi:10.1109/IJCNN52387.2021.9533342
- 468 Krauss, P., Schuster, M., Dietrich, V., Schilling, A., Schulze, H., and Metzner, C. (2019a). Weight statistics
469 controls dynamics in recurrent neural networks. *PLOS ONE* 14, e0214541. doi:10.1371/journal.pone.
470 0214541
- 471 Krauss, P., Zankl, A., Schilling, A., Schulze, H., and Metzner, C. (2019b). Analysis of structure and
472 dynamics in three-neuron motifs. *Frontiers in Computational Neuroscience* 13, 1–6. doi:10.3389/fncom.
473 2019.00005
- 474 Kuśmierz, , Ogawa, S., and Toyoizumi, T. (2020). Edge of Chaos and Avalanches in Neural Networks
475 with Heavy-Tailed Synaptic Weight Distribution. *Physical Review Letters* 125, 028101. doi:10.1103/
476 PhysRevLett.125.028101
- 477 L. D. Landau, E. L. (1980). *Statistical Physics*, vol. 17 (Course of theoretical physics), 3rd edition edn.
- 478 Lavis, D. A., Kühn, R., and Frigg, R. (2021). Becoming Large, Becoming Infinite: The Anatomy of
479 Thermal Physics and Phase Transitions in Finite Systems. *Foundations of Physics* 51, 1–69. doi:10.
480 1007/S10701-021-00482-5/FIGURES/9
- 481 Lewin, R. and Bak, P. (1993). Complexity: Life at the Edge of Chaos. *American Journal of Physics* 61,
482 764–765. doi:10.1119/1.17163

- 483 Maass, W., Natschläger, T., Markram, H., Maass, Natschlager, and Markram (2002). Real-time Computing
484 Without Stable States: A New Framework for Neural Computation Based on Perturbations. *NEURCOMP: Neural Computation* 14, 2531–2560. doi:10.1162/089976602760407955
- 485 Mamun, M. S. I., Ghorbani, A. A., and Stakhanova, N. (2016). An Entropy Based Encrypted Traffic
486 Classifier. In *Information and Communications Security. ICICS 2015. Lecture Notes in Computer Science*. vol. 9543, 282–294. doi:10.1007/978-3-319-29814-6{__}23
- 487 Merolla, P. A., Arthur, J. V., Alvarez-Icaza, R., Cassidy, A. S., Sawada, J., Akopyan, F., et al. (2014). A
488 million spiking-neuron integrated circuit with a scalable communication network and interface. *Science*
489 345, 668–673. doi:10.1126/science.1254642
- 490 Metzner, C. and Krauss, P. (2022). Dynamics and Information Import in Recurrent Neural Networks.
491 *Frontiers in Computational Neuroscience* 16, 1–15. doi:10.3389/fncom.2022.876315
- 492 Rosin, D. P. (2015). *Dynamics of Complex Autonomous Boolean Networks*. Springer Theses (Cham:
493 Springer International Publishing). doi:10.1007/978-3-319-13578-6
- 494 Schrauwen, B., Verstraeten, D., and Van Campenhout, J. (2007). An overview of reservoir computing:
495 Theory, applications and implementations. In *ESANN 2007 Proceedings - 15th European Symposium on
496 Artificial Neural Networks*. 471–482
- 497 Seifert, J. and Reggia, J. A. (2015). Lambda and the Edge of Chaos in Recurrent Neural Networks. *Artificial
498 Life* 21, 55–71. doi:10.1162/ARTL{__}a{__}00152
- 499 Sherrington, D. and Kirkpatrick, S. (1975). Solvable model of a spin-glass. *Physical Review Letters* 35.
500 doi:10.1103/PhysRevLett.35.1792
- 501 Snyder, D., Goudarzi, A., and Teuscher, C. (2013). Computational capabilities of random automata
502 networks for reservoir computing. *Physical Review E - Statistical, Nonlinear, and Soft Matter Physics*
503 87, 1–8. doi:10.1103/PhysRevE.87.042808
- 504 Tanaka, G., Yamane, T., Héroux, J. B., Nakane, R., Kanazawa, N., Takeda, S., et al. (2019). Recent
505 advances in physical reservoir computing: A review. *Neural Networks* 115, 100–123. doi:10.1016/j.
506 neunet.2019.03.005
- 507 Zhou, J. and Zeng, X. (2022). Physical Layer Secret Key Generation for Spatially Correlated Channels
508 Based on Multi-Task Autoencoder. *2022 7th International Conference on Intelligent Computing and
509 Signal Processing, ICSP 2022*, 144–150doi:10.1109/ICSP54964.2022.9778422

512 *Supplementary Material*

7 THE EXPERIMENTS

513 This article proposes two sets of experiments: in the first setting, one is interested in the free time evolution
 514 of the reservoir without input ($u_i = 0$). The second set is devoted to the measurement of the capacity of the
 515 reservoir to execute two tasks.

516 7.1 Free running network

517 Both experiments in this section are based on the same simulation, and do not require the input and
 518 readout layers:

- 519 1. At time $t = 0$ the network state is randomly initialized with provided *seed*, and a fixed 20% of active
 520 nodes ($x_i = 1$).
 521 2. Then the network is let run for a duration $D = 2000$ time steps.

522 For each value of σ^* , we generate 100 reservoirs, i.e. reservoirs having all the same architecture but
 523 different weights. We consider two ways to perform statistics.

524 **Statistics over many reservoirs** (section 3.1).

525 Each **reservoir** is run once in a *free run simulation*. We report the result of 90 values of $\sigma^* < 0$, 110
 526 values of $\sigma^* > 0$, and 80 for $\mu = 0$, for a total of 28,000 simulations.

527 **Statistics of reservoirs** (section 3.2).

528 Each **reservoir** is run 100 times with different initial conditions. We report the result of 80 values of σ^*
 529 for each sign, for a total of 1,600,000 simulations.

8 THE CONTROL PARAMETER VALUES

530 Below are the parameter values for the experiment of free running (see methodology in S7.1):

	Start	End	Step
531	0.01	0.06	0.001
	0.06	0.1	0.0007
	0.07	0.1	0.001
	0.1	0.2	0.01
	0.2	1	0.1
	1	11	1

Table 1. Values of $\sigma(W)$ for the first experiment, $\mu = -0.1$.

	Start	End	Step
	0.01	0.07	0.001
	0.07	0.2	0.01
	0.2	0.5	0.02
	0.5	1	0.1
	1	11	1

Table 2. Values of $\sigma(W)$ for the first experiment, $\mu = 0.1$.

532 8.1 Performance of tasks

533 All experiments in this section test the performance in a task, where learning is required for the readout
 534 layer. For all tasks, the following framework is applied. Assuming that F is the reservoir, the relationship

535 between the input time series $u(t)$ and the output layer y is $y(t) = F(u(t))$. The goal here is to learn the
 536 target $T(t)$, such that $y(t) = T(t)$ and the target is set to:

$$T(t) = u(t + \delta) \quad (8)$$

537 Here, δ is an integer which represents a number of time steps. This parameter serves the general purpose of
 538 setting the type of task:

539 • **Memory task** for $\delta < 0$, the reservoir output must reproduce the input received in the past.

540 • **Prediction task** for $\delta > 0$, the network output must produce an input not yet seen by the reservoir.

541 The (integer) parameter δ also sets the difficulty of the task: the higher in absolute value, the more
 542 demanding it is.

543 **White noise memory** (section 4). $u(t)$ is a zero mean, unit variance white i.i.d noise. Successive inputs
 544 are uncorrelated, so prediction is not involved, only memory. We report results for $\delta \in \{-14, -10, -6, -2\}$
 545 (see figure 4.A for an illustration).

546 **Prediction of Mackey-Glass series** (section 4). $u(t)$ is the Mackey-Glass time series Hajnal and Lörincz
 547 (2006), which is common to benchmark reservoir computational capabilities. It is given by the following
 548 dynamical equation:

$$x_{t+1} = ax_t + \frac{bx_{t-\tau}}{c + x_{t-\tau}^d} \quad (9)$$

549 We choose $a = 0.9$, $b = 0.2$, $c = 0.9$, $d = 10$ and $x_0 = 0.1$. The dynamic of this equation can be controlled
 550 by varying τ : as τ increases, the time series evolves from periodic ($\tau = 5$) to chaotic ($\tau = 28$), with a
 551 continuous increase in complexity in between. Results are for a fixed $\delta = 10$ and $\tau = \{5, 15, 20, 28\}$ (see
 552 figure 4.B for an illustration).

553 8.2 Training

554 The two tasks follow the same protocol for training the readout:

555 • The network receives the input u for duration $D = 2000$ time steps.

556 • The first 500 time steps are discarded and considered transients. This value is empirically obtained,
 557 adapted from the signal at hand, and coupled to a convergence test for permanent regime detection.

558 • The training is performed on the following 1500 time steps on the concatenated in-time reservoir
 559 outputs, using the optimization procedure described in 2.3.

560 Each experiment consists in 40 values of σ^* , 100 reservoirs per σ^* value, and each network is run 5 times
 561 with different randomly tossed inputs (i.e., 40,000 simulations). Each training is performed for 4000 epochs
 562 (with a total of 640,000,000 training epochs).

563 8.3 Performance

564 The metrics of performance are given by the *Pearson correlation coefficient* between the output and the
 565 target (each of length 1500). A perfect match corresponds to a correlation of 1 while 0 means an output of
 566 the network is not better than random.

9 MEASURE OF NETWORKS DYNAMICS

To evaluate the reservoir dynamics, we used the most straightforward measure one can imagine: the *activity*, which we defined as the sum of all spikes at each given time step, see supplementary material 10. We will take some time to make the reader appreciate the usefulness of such an approach. The sum of binary spikes is mathematically equivalent to how the magnetic field of spins in the ISING models Ising (1925) is computed. In ISING, the electron spins are modelled as miniature magnets that can take binary values $[-1, 1]$, which flip with some probability depending on temperature and the coupling with other spins. The ISING model is one of the closest physical models to neural networks. In fact, it has been widely used to design neural networks, for example, in the famous Hopfield network Hopfield (1982) or the Boltzmann machine Sherrington and Kirkpatrick (1975). So one could argue that our activity signal is close to what Magnetoencephalography (MEG) is for brain activity Hämäläinen et al. (1993).

Since this analysis does not depend on the micro-constituents, we make the case that the methodology performed in this article is easily transferable to other neural models and to other fields, such as neurosciences, physics, and the study of complex dynamical systems.

Activity: we define $A(t)$, the averaged activity of the network at time t , and for simplicity we will refer to it as *activity*. It is the normalized sum of all neural states $x_i(t)$:

$$A(t) = \frac{1}{N} \sum_{i=1}^N x_i(t)$$

Steady state of reservoir: In the main text (part 3.1), we defined the steady state as A for ease of notation, here for the sake of clarity, we define the steady activity A_s of free-running reservoirs during $D = 2000$ time steps, as $A_s = A(t \geq D/2)$, the activity of the last $D - D/2 = 1000$ time steps of free running simulations.

10 METRICS

10.1 Permanent regime statistics:

here are two statistical analyses we perform on the measure of the steady state activity A_s of a given reservoir, where (\cdot) represents the time-average over a quantity, and $\delta A(t) = A(t) - \bar{A}$:

- Permanent regime time-average:

$$\bar{A}_s = \frac{2}{D} \sum_{t=D/2}^D A(t)$$

- Permanent regime time-variance:

$$\overline{\delta A_s^2} = \frac{2}{D} \sum_{t=D/2}^D (A(t) - \bar{A}_s)^2$$

Average over reservoirs of permanent regime statistics: in the *first experiment* (see results in section 3.1), for each value σ^* , we compute the average (over reservoirs generated with 100 different seeds) of the permanent regime *average* and *variance* (overtime time step t). Here A_s^r denotes the stationary activity of the reservoir of index r generated with $seed = r \times 100$, for a total number of reservoir $R = 100$. We

593 compute the average over reservoirs of the permanent regime statistics, where the back $\langle \cdot \rangle$ denotes the
 594 average over reservoirs:

- Average over reservoirs of the permanent regime average:

$$\langle \bar{A}_s \rangle = \frac{1}{R} \sum_{r=1}^R \bar{A}_s^r$$

- Average over reservoirs of the permanent regime variance:

$$\langle \overline{\delta A_s^2} \rangle = \frac{1}{R} \sum_{r=1}^R \overline{(\delta A_s^r)^2}$$

595 **Statistics of the BiEntropy:** the BiEntropy solves one important limitation of the Shannon entropy,
 596 regarding the evaluation of binary words: as an example, let us take these two binary words "01010101"
 597 and "10110010". Although one is fully periodic and the other is somewhat random, they both have the
 598 same probability of occurrence of 1's and 0's; hence they have the same Shannon entropy. The Shannon
 599 entropy is thus insufficient to inform on the regularity versus the disorder of binary words. In contradiction,
 600 the binary entropy has been designed to discriminate patterns that the Shanon entropy could not Blackledge
 601 and Mosola (2020). We argue that in our context this metric is perfectly fitted to evaluate the binary words
 602 of spike time patterns. Since phase transition in such systems are known to be between an ordered and
 603 disordered phase, while the critical regime, also known as the edge of chaos, is supposedly a mixture of
 604 both. One property of particular interest to us regarding that metric, is that it is bounded between between
 605 0 (for perfectly ordered words), and 1 (totally disordered).*

606 • BiEntropy of permanent regime: the BiEntropy H_b is computed on binarized steady activity δA_s . First,
 607 we subtract the mean $A_s - \bar{A}_s$, and then all positive values are clamped to one and negative values to
 608 zero, resulting in a binary sequence. The H_b is then computed on this sequence after converting it to a
 609 string.

- Average over reservoirs of the permanent regime BiEntropy:

$$\langle H_b \rangle = \frac{1}{R} \sum_{r=1}^R H_b^r$$

- Variance over reservoirs of the permanent regime BiEntropy:

$$\langle \overline{(\delta H_b)^2} \rangle = \frac{1}{R} \sum_{r=1}^R (H_b^r - \langle H_b \rangle)^2$$

610 NB: given that neuron states are binary, one could wonder why employing a binarized version of a
 611 continuous variable like A . The reason is twofold: 1. the number of neurons in the network is $N = 10000$.
 612 Therefore, computing H_b on all neurons would be extremely costly. As such, reducing the number of
 613 neurons would be crucial, though it would necessitate a criterion for selection. This poses the risk of
 614 missing important information or introducing biases. 2. This would not be applicable in many real-world

* For example, the word "01010101" has $H_b = 0.0078$, and the word "10110010" has $H_b = 0.7596$. A convenient way to discriminate both words.

615 applications where access to the micro-constituents of the reservoir is difficult or even impossible. As such,
616 we ensure our methodology is easily transferable to other areas comprising non-invasive studies of the
617 brain.

11 CLASSIFICATION OF ATTRACTORS

618 In this section, we provide a more grounded explanation of the choice of attractor categories. In the main
619 text (part 3.2), we developed a scheme to categorize activities by their respective attractor. Fig. 4 showed
620 the histograms of attractors as a function of σ^* , and in this section, we provide a refined version of these
621 statistics by adding two more categories of attractor:

- 622 • *Saturated attractors*: The steady activity is saturated when all neurons are active at all times.
623 • *Non-trivial*: Any signal whose category of dynamics changes over time and that does not fit in
624 previously mentioned types is considered non-trivial. This comprises cases where during the time
625 window considered, activity suddenly changes from one type of dynamic to another.

626 We show in Fig. 7 examples of the various activities belonging to each category, *No-Activity* and *Fix* (**A**),
627 *Cyclic* (**B**), *Chaotic* (**C**), and lastly, *Non-Trivial* (**D**). In the following paragraphs, we explain in more detail
628 some specificities of the *fixed* point attractor category and the reason why de did not treat the *Non-trivial*
629 case separately from the chaotic ones.

630 First, we must mention that the *fixed* point attractor category could, in theory, encompass the *extinguished*
631 and *saturated* cases as well. This is because they all fit inside the definition of a time derivative of zero. The
632 reason why we separated inactive reservoirs from the two others comes from percolation theory Coniglio
633 et al. (1976): formally, a reservoir has not percolated if the activity does not spread to infinity in space
634 and/or time. While at the percolation threshold, activity will start to propagate indefinitely. We make the
635 case that the percolation threshold, which does not coincide here with the critical points, constitutes another
636 type of transition Cohen et al. (2010), from inactive, to active, hence the distinction. This is visible in
637 Fig. 5.A, as the fixed point attractors appear a bit before the *cyclic* ones, around $\sigma^* \sim 0.5$.

638 Second, in Fig. 7.F, we can see that the transition from *Saturated* to *Fix* attractor happens very early (in
639 terms of σ^*), compared to the rest of the attractors. So early, in fact, that it is not part of the phase transition.
640 As you might recall, the analysis performed in part 3.1 revealed that this region has a zero variance of both
641 activity and BiEntropy. We conclude that the transition from *Saturated* to *Fix* is not related to a change of
642 dynamics but only to a change in amplitude. As a result, we have chosen not to differentiate the two.

643 Thirdly, as one can clearly see in both Fig. 7.E and F, the *Non-trivial* dynamics are very rare. As such,
644 it is worth mentioning that in the analysis performed in S13, where we categorize reservoirs depending
645 on their dominant attractors, not a single reservoir exhibits a dominance of *Non-Trivial* dynamics. This
646 is important because it means this category of attractors is irrelevant for finding correlations between
647 dominant attractors and performance.

12 DIVERSITY OF RESERVOIR ATTRACTOR DISTRIBUTIONS

648 We compute the Shanon entropy H_s , with the goal of quantifying how varied are the attractor distributions
649 of given reservoirs. Typically, if a reservoir activity always falls into one attractor, irrespective of the initial
650 state, the Shanon entropy will give 0. On the other hand, the maximum entropy is obtained for a uniform

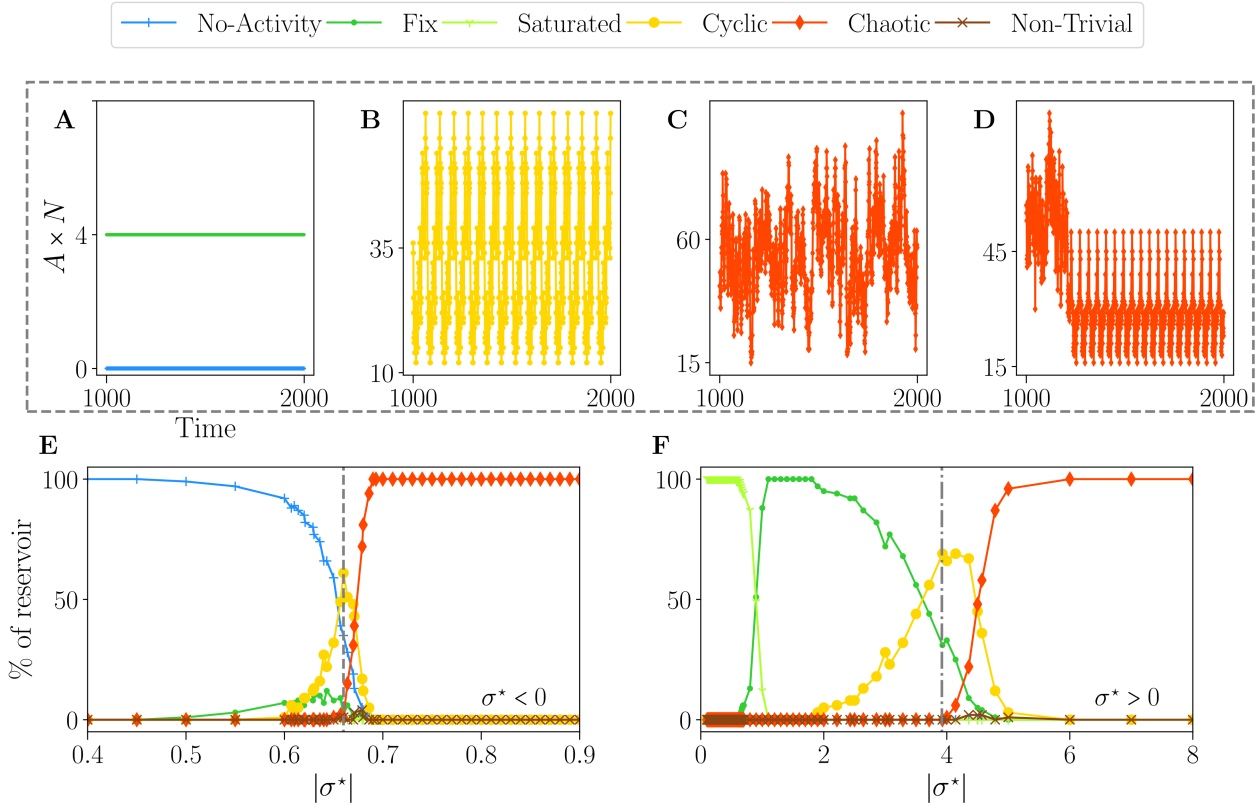


Fig. 7. The statistics of the dynamics of free running simulations. For each value of σ^* , 100 reservoirs are run once (see methodology 7.1). The resulting activities are classified into the respective category of attractors, of which we can see an example: **A** no-activity (+), fix (•); **B** cyclic (○), **C** chaotic (◆), and **D** non-trivial (×). The percentage of trials (or activities) belonging to each category of attractors is plotted against the control parameter σ^* . **A** the phase transition for $\sigma^* < 0$, and **B** the phase transition obtained with $\sigma^* > 0$. In both cases, we zoom on the critical regions since the ordered, and chaotic regimes have constant statistics.

651 distribution where each attractor is obtained 1/4 of the time, and $H_s^{max} = -\log(1/4)$. The Shanon Entropy
652 is therefore normalized by its maximum value and averaged over the 100 reservoir of each value of σ^* .

653 To quantify reservoir dynamics diversity, we plotted the average normalized entropy of reservoir attractor
654 distributions, $\langle H_s / H_s^{max} \rangle$, against the control parameter for $\sigma^* < 0$ (**A**) and $\sigma^* > 0$ (**B**). The shaded area
655 represents one standard deviation. Lower values of this quantity indicate a stronger dominance of one
656 attractor. Outside of the critical region, initial conditions are irrelevant, and reservoirs always converge to a
657 single attractor. The region where $\langle H_s \rangle$ increases correspond precisely to the region where the BiEntropy,
658 shown in Fig. 8, is nonzero. In this region, different reservoirs may lead to different attractors. There is
659 significantly more entropy, i.e. more competition between attractors, for $\sigma^* < 0$.

660 The higher variance in H_s also implies increased reservoir-to-reservoir variability. This variability is
661 more pronounced for $\sigma^* < 0$, with the average entropy exceeding 0.25 near the critical point and the
662 shaded area approaching 0.5. For $\sigma^* > 0$, reservoirs generally exhibit stronger dominant attractors, as
663 the standard deviation never surpasses 0.25. Despite these differences, the normalized entropy remains
664 consistently below 0.5 for all values of σ^* , irrespective of the sign. This value approximately corresponds
665 to an attractor distribution where one attractor dominates 80% of the initial conditions, indicating that most
666 reservoirs possess a peaked distribution with a predominant attractor.

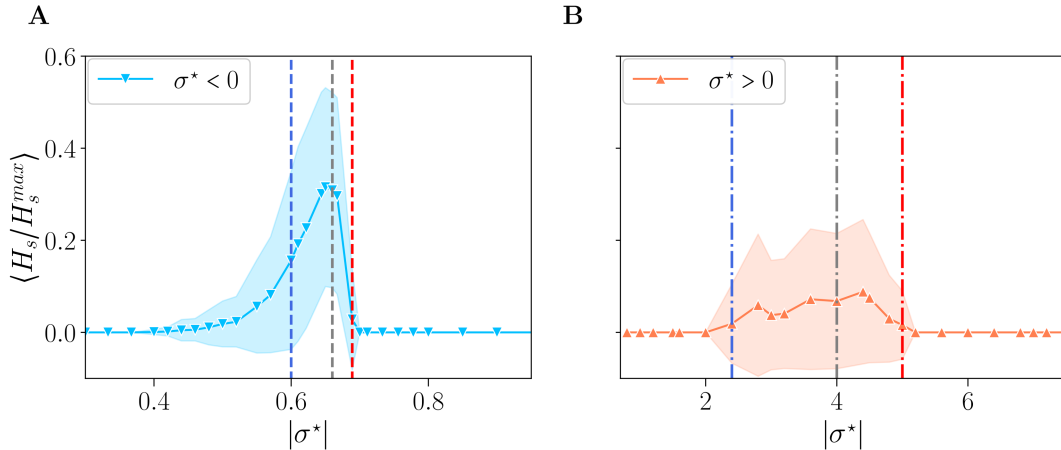


Fig. 8. The normalized Shanon entropy of individual reservoir attractor distributions. **A** and **B**: The average over reservoirs entropy of the entropy H_s versus the control parameter $|\sigma^*|$, for $\sigma^* < 0$ (**A**) and $\sigma^* > 0$ (**B**).

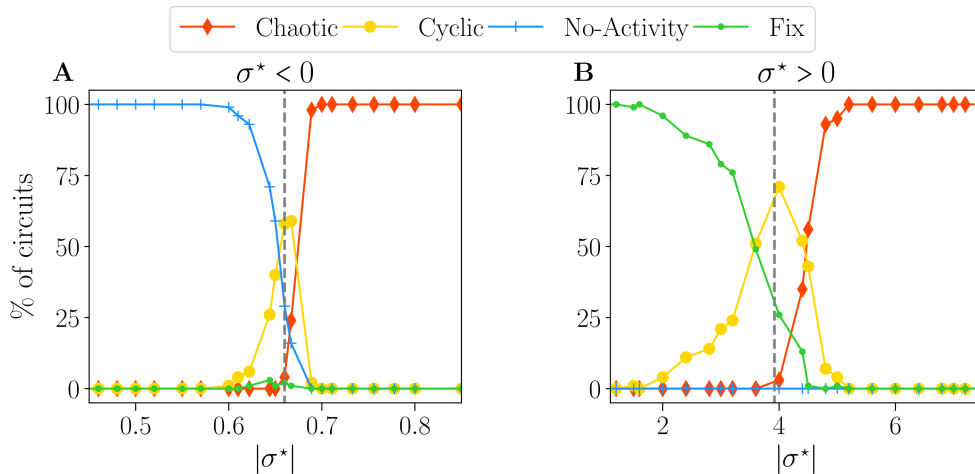


Fig. 9. The statistics of reservoir dominant attractors. The statistics of the dynamics of free-running simulations. For each value of σ^* , 100 reservoirs are run 100 times, with different initial conditions (see S7.1). The resulting activities are classified into the category of attractors: no-activity (+), fix (●), cyclic (○), and chaotic (◆). The statistics of reservoirs with specified dominant attractor is plotted against the control parameter σ^* . **A** the case $\sigma^* < 0$, and **B** displays $\sigma^* > 0$.

13 STATISTIC OF DOMINANT ATTRACTORS

667 Fig. 9 displays the statistics of the dominant attractors of each of the 100 reservoirs generated by σ^* values.
 668 As one can note, the statistics are also unchanged from Fig. 4. Taken together, these results indicate strong
 669 statistical robustness, as averaging over reservoirs is almost equivalent to averaging reservoirs themselves.